

Biomechanical Modeling of the Pelvic System: Improving the Accuracy of Prostate Lesions Location in MRI–TRUS Fusion

Muhammad Qasim

Universitat Rovira i Virgili

Dolors Puigjaner

Universitat Rovira i Virgili

Joan Herrero

Universitat Rovira i Virgili

Josep M. López

Universitat Rovira i Virgili

Josep R. Garcia–Bennett

Bellvitge University Hospital

Carne Olivé

Universitat Rovira i Virgili

Gerard Fortuny (✉ gerard.fortuny@urv.cat)

Universitat Rovira i Virgili

Research Article

Keywords: Magnetic Resource Imaging (MRI), Prostate lesions, Code Aster, Transrectal ultrasound (TRUS) probe, TRUS-guided biopsy

Posted Date: August 18th, 2021

DOI: <https://doi.org/10.21203/rs.3.rs-658749/v1>

License: © ⓘ This work is licensed under a Creative Commons Attribution 4.0 International License.

[Read Full License](#)

Abstract

Background: An accurate knowledge of prostate lesions relocation during biopsy is of great importance to prevent mispositioning of the needle and thus reduce the chance of faulty biopsy results (false negatives). Prostate lesions are visible in magnetic resonance images (MRI) but it is difficult for the practitioner to locate them at the time of performing a transrectal ultrasound (TRUS) guided biopsy. In this study, we present a new methodology that predicts both prostate deformation and lesion migration during the biopsy.

Methods: A three-dimensional (3-D) anatomy model of the pelvic region, based on medical images, is constructed. A finite element (FE) simulation of the organs motion and deformation as a result of the pressure exerted by the TRUS probe was carried out using the code_aster open source software. Initial positions of potential prostate lesions prior to biopsy are taken into consideration and the final location of each lesion is targeted in the FE simulation output.

Results: Our 3-D FE simulations show that the effect of the pressure exerted by the TRUS probe is twofold as the prostate experiences both a motion (in the absolute frame of reference) and a deformation of its original shape. We targeted the relocation of five small prostate lesions when the TRUS probe exerts a force of 30 N on the rectum inner wall. The distance traveled by these lesions ranged between 5.6 and 13.9 mm. Moreover, we showed that as a result of the deformation of the prostate the resulting lesion migration might be very difficult to predict if the biopsy practitioner has to rely exclusively on a visual comparison of axial or sagittal prostate slices taken from MRI and TRUS images.

Conclusions: The preliminary results presented here show that our new methodology can be of great help for improving the prediction of cancerous lesions location when a TRUS guided biopsy is performed. Moreover, the new methodology is completely developed on open source software, which means that its implementation would be affordable even for healthcare providers with small budgets.

1. Background

Cancer sets up a massive burden on societies and Prostate Cancer (PCa) is the tumor with the highest incidence in men in the UE and third in mortality in men [1]. In 2018, approximately 1.3 million of PCa new cases were registered (representing around 7.1% of total cancer cases) and almost 359,000 deaths were associated to PCa cancer all around the world [2, 3]. Prostate cancer incidence and mortality rate increase with age, being the average age of diagnosis 66 years old [4].

Prostate is located in the center and lower part of the pelvis, just beneath the bladder with which it is in contact. The puborectalis and pubococcygeus muscles of the levator ani muscle along with other pelvic floor muscles provide primary support to the prostate (see Fig. 1). PCa typically arises in the peripheral zone of the gland and can extend to a significant size before involving other organs of the male genitourinary system [5]. Certain prostate lesions that are missed by PSA screening can be detected through a DRE test [6]. Urologists typically use PSA and DRE tests to screen for prostate cancer. If

prostate cancer is suspected, as it is the case when values of PSA above 4.0 ng/ml are obtained, a transrectal ultrasound (TRUS) scan is usually performed [7, 8]. TRUS allows radiologists to determine the size, shape and glandular structure of the prostate [9].

Cancerous prostate tissue is stiffer than benign and normal tissue [10, 11, 12], however, manual palpation of cancerous lesions can be difficult when the elastic properties of unhealthy tissue are similar to those of a healthy one [13]. Furthermore, a DRE test does not provide any statistical or numerical information, and therefore its effectiveness depends on the skills and expertise of the physician. The transrectal ultrasound (TRUS) guided biopsy is commonly used in clinical practice to diagnose prostate lesions because it is a safe and efficient procedure [14]. It consists in the insertion of a needle through the rectum wall and towards the prostate to obtain a sample of potentially cancerous tissues. The procedure is conducted using ultrasound images that are obtained by an endorectal probe. The pressure of the TRUS probe on the rectum wall results in motions and deformations of the surrounding pelvic organs, including the prostate itself.

The motion and deformation of the prostate during TRUS guided biopsy makes it difficult to know in advance the location of potential prostate lesions. Actually when using this procedure practitioners can only expect to know rough estimations for the lesions locations. Consequently, multiple biopsy samples are required in order to target one single lesion [15], but an increase in the number of biopsy samples can augment undesirable associated complications such as rectal bleeding, hematospermia (blood in semen), hematuria (blood in urine), and infections [16]. In the last few years there has been a tendency to include information from magnetic resonance images (MRI) to guide the prostate biopsy process. As MRI gets more and more sensitive in the detection of small lesions, sampling those small lesions becomes increasingly dependent upon the targeting accuracy of the practitioner [17]. In attempting to address this weak point several commercial platforms for guided biopsies have been launched into the market. According to Warlick et al. [18] guided biopsy platforms that include MRI images can be classified into the following three categories: MRI-compatible prostate biopsy systems, MRI-TRUS fusion biopsy systems and Robotic in-bore MRI biopsy systems. All these platforms have their pros and cons and none of them seems to be a definitive solution for the exact location of lesions inside the prostate during guided biopsy[18]. Fusion biopsy is dependent upon registration and it is very challenging to achieve accurate registration due to the large appearance difference between TRUS and magnetic resonance images. Moreover, the integration of several different technologies and devices into a platform is a costly process and consequently the acquisition of one of these commercial guided biopsy platforms is not affordable for all healthcare providers.

Several previous studies aimed to improve the accuracy of prostate lesions location during a TRUS guided biopsy. Different perspectives were applied in these studies. Some authors [19, 20, 21] proposed statistical and biomechanical methods to investigate the prostate deformation under different ultrasound probe insertion conditions. In particular, Wang et al. [19] provided patient-specific biomechanical parameters, acquired from ultrasound elastography, for the prostate transitional (TZ) and peripheral (PZ) zones for a data set with twelve patients. Other authors [20, 21] used finite element (FE) based statistical

motion models (SMM) to estimate the shape adopted by a prostate when it was deformed because of TRUS probe pressure. Baratha et al. [22] proposed a deformable image registration system based on a biomechanical 3-D FE modeling with linear elastic properties for the prostate. Marchal et al. [23] implemented a discrete modeling method to simulate the displacement and deformation of the prostate due to both internal interactions between organs and external interactions between organs and surgical tools, such as the needle. Other studies [24, 25, 26], performed in the context of prostate radiotherapy, provided also interesting information on how to address the challenging problem of motion and deformation of prostate.

In this study we present an alternative methodology that can improve accuracy in the location of prostate lesions during a TRUS guided biopsy. Our methodology is entirely based on open source software and therefore it can be implemented with a comparatively low cost. The main goals of this study are:

- The integration of an accurate and realistic 3-D geometry of the pelvis region with the constitutive properties of the tissues involved into a FE model.
- The use this FE model to simulate the biomechanical response of prostate to the pressure applied by the TRUS probe on the rectum wall during a TRUS guided biopsy.
- The prediction of the actual location of prostate lesions during a TRUS guided biopsy.

2. Methods

The geometry model of the male pelvis region used in the current study is shown in Fig. 1. It is a realistic model that includes pelvic bones (hip and sacrum bones), pelvic muscles (obturator internus, obturator externus, iliococcygeous, pubococcygeous, puborectalis and vesical muscles), anus, rectum, bladder and the prostate transitional zone (TZ) and peripheral zone (PZ). Our geometry model is based on computerized tomography (CT) images available in the BodyParts3D database for anatomy [27]. This dictionary-type anatomical database provided (3-D) triangular surface meshes for each of the individual elements involved in our male pelvis model. These surface meshes were conveniently refined and modified (undesirable intersections of adjacent elements were removed) using home-made software together with CGAL libraries [28] to obtain physically consistent meshes. The consistent surface meshes, with a total of 180,766 triangles, were then uploaded into the Gmsh open source software [29] where 3-D tetrahedral volume meshes were obtained and optimized using the Netgen algorithm. These volume meshes were finally compounded into a single computational mesh consisting of 655,355 tetrahedra.

Numerical simulations were performed using the Code Aster open source FE software [30]. In the simulations we replicated as closely as possible the real conditions of the clinical practice of a TRUS guided biopsy. We assumed that a force of 30 N was orthogonally exerted onto a surface patch of the rectum wall whose area was 258 mm² (an sketch can be seen in the inset of Fig. 1b). The patch was devised to be representative of the average shape and size of the contact region of the probe and the rectum wall. In addition, fixed (zero deformation) boundary conditions were prescribed for the sacrum and hip bones.

We assumed an isotropic linear elastic behavior for all the tissues included in our model. To describe a linear elastic behavior two parameters are needed: the Young's modulus, E , which measures the stiffness of the material and the Poisson's ratio, η , which measures the relative volume change [37]. It is known that the right setting of the biomechanical parameters is a key point to obtain reliable results in the numerical simulations. However, the choice of these parameters is not an easy task since there is a large inter-subject variation of the mechanical properties of biological tissues, and prostate tissue is not an exception [19]. In the present study, the Young's modulus, E , for TZ and PZ tissue were chosen as those obtained from shear wave elastography by Wang et al. [19] for their patient case 6. Following Krouskop et al. [10] the Poisson ratio η for prostate tissues was set to 0.495. The material properties for all the other involved tissues were also obtained from the literature [31, 32, 33, 35, 36] and their specific values are summarized in Table 1.

The main results of a FE simulation are the deformation and stress fields. In the present study we focused on the calculated deformation field. To simulate the displacement of very small lesions within the prostate, i.e., the ones that are hardest to register with the fusion procedure, some particular mesh nodes were selected in the original geometry and their displacement were then tracked by measuring their resulting location in the deformed geometry.

3. Results

Figure 2 shows the predicted deformations experienced by the rectum, the bladder and the prostate when the TRUS probe exerts a force of 30 N on the rectum inner wall. The region where the probe exerts the force, that is, the anterior part of the rectum and the posterior part of the prostate (see Fig. 1a), is the one that experiences the highest deformation. The deformed rectum in turn pushes against the prostate producing its displacement towards the ventral region ($-Y$) together with a significant non-uniform deformation of the TZ and PZ geometry. The maximum displacements along the $-Y$ direction for the rectum, TZ and PZ contours in the plane of Fig. 2 were respectively of 13.5 mm, 11 mm and 12 mm. At the same time, the bladder region that was in contact with the prostate was deformed and cranially displaced (Z direction) approximately 9 mm. Note that the high difference in stiffness of bones and muscles contributes to the generation of non uniform deformations of the rectum, the bladder and the prostate. To simulate the displacement of small lesions in the prostate we selected five different nodes, as defined in the two leftmost columns of Table 2 and sketched in Fig. 3. Note that nodes N1, N3, N4 and N5 are located near the outer surface of the PZ whereas the node N2 is located within the TZ.

Figure 4 shows superimposed projections, in the sagittal plane, of the original prostate geometry and the deformed geometry when the TRUS probe exerts a force of 30 N. Comparison of original and deformed surface contours reveals the two main effects of the TRUS probe pressure, namely a motion (a displacement in the absolute frame of reference) and a deformation (a change in volume and shape) of the prostate gland. The displacements of the selected nodes are also portrayed in Fig. 4. For the sake of clarity, we have replicated the same surface contour plot five times showing only one of the nodes in each plot. The detailed information of node displacements along each of the 3-D coordinate-axes, as well as

its magnitude, are presented in Table 2. The distance traveled by the nodes ranges between 5.20 and 13.91 mm, being the N1 node the one experiencing by far the highest displacement. This fact is not surprising considering that N1 is the node located closer to the rectum, that is, it lies close to the prostate surface region most directly affected by the rectum motion, which is in turn induced by the probe pressure. On the other hand, the lowest displacement of the N3 node may be attributed to the restraint imposed by the puborectalis and pubococcygeus muscles. Note that the deformation induced by the probe also implies a strong departure from symmetry with respect to the midcoronal plane. In simpler words, the original prostate shape in Fig. 4 still recalls what would be the surface of an idealized ellipsoid whereas the deformed contour features a far more irregular shape.

State-of-the art of MRI-TRUS fusion platforms rely on the procedure known as registration, which consists in the superposition of slices containing the original lesion in the original MRI image set and the corresponding slices in the TRUS image set. Registration is aimed to facilitate the practitioner work during biopsy by removing (or at least greatly reducing) one of the outputs of TRUS, i.e., prostate motion (see Fig. 4). Ideally, the two superimposed slices (from MRI and TRUS) would show similar shapes so that the practitioner conducting the biopsy would estimate with a reasonable degree of accuracy the location of the target lesion in the deformed geometry. Following the particular approach proposed by Igarashi et al. [38], Fig. 5 shows superimposed slices of the original and deformed prostate in a polar coordinate framework together with the original and displaced locations of the control node N1 in the axial plane. That is, Fig. 5 intends to approximate the type of representation that a MRI-TRUS registration procedure would generate when intending to track the N1 node. The idea behind the polar coordinate framework is to determine the origin of the polar system in the original (undeformed) slice, the corresponding origin in the deformed slice and then to apply a translation of the latter origin into the former one, which results in the superimposition of both images.

During a biopsy, the first question for the practitioner would be what particular slice has to be visualized in the TRUS image. In Fig. 5a we simulate the most obvious choice for an axial slice, i.e., keeping the same vertical location ($Z = 0$) wherein the lesion was observed in the original MRI images. We see clearly in this figure that even after registration (superimposition of slices) the large deformation experienced by the prostate makes the final slice quite different from the initial one. At first sight, however, it seems that given the initial location of N1 in the axial plane its final location (N1') would not be difficult to estimate. In this respect, the N1 node appears to be rather favorably placed, as it is very close to the prostate external wall and it lies in the midsagittal ($X = 0$) plane. Note that, as will be discussed below, we have plotted in Fig. 5a not the real N1' 3-D location but just its projection in the axial plane. Our biomechanical model predicts a small leftwards displacement of N1 as a result of the deformation, which is consistent with the fact that we have worked with a realistic geometry, that is, a real human body will never be 100% symmetric. The sagittal slices superimposed in Figure 5c show that the biggest source of error in the final N1' location, when sought in the original ($X = 0$) axial plane, is in the normal coordinate (Z). Our biomechanical FE simulation predicts that the final N1' location is not in the original axial location ($Z = 0$) but in the plane with $Z = 5.16\text{mm}$ (see Table 2). This is taken into account in Fig. 5b, where registration is performed using the proper slice for N1'. Note that both axial polar plots in Figs. 5a and 5b are quite

similar. Thus, for the example considered here (for the N1 node) the bright side is that the practitioner would probably produce a good guess of the X and Y coordinates of the lesion in the TRUS image regardless of the particular axial plane being visualized. On the minus side, as clearly shown in Fig. 5c, we have that even with an accurate projection of the lesion in the axial plane a large error could be made in the estimate of its axial location (Z). The example shown in Fig. 5 therefore illustrates the fact that it might be quite difficult to estimate the final lesion location using visual inspection alone. The biomechanical approach presented in this study therefore provides an extra layer of knowledge that might well greatly improve in the future the accuracy in the MRI-TRUS fusion procedures.

4. Discussion

In this study we have restricted our FE simulations to the tracking of very small prostate lesions, which can be assimilated to a node in the computational mesh. The present methodology could however be easily extended to track the deformation and displacement of larger lesions (tumors), by defining a group of volume elements for each tumor and assigning a different set of properties (E, η) for the tumoral tissue.

Our results revealed that a 30 N force exerted by the TRUS probe on the rectum wall led to a significant deformation of the TZ and PZ. This significant deformation can pose difficulties to image registration, a key component of MRI-TRUS fusion platforms. From a radiological standpoint, it is important that lesions in the posterior region of the prostate (N1) and those in the middle third (N2) are the ones experiencing the largest displacements. Moreover, lesions located laterally (N3), anteriorly (N5) or in the apex level (N4) are the ones that more often need to be tracked using MRI-TRUS fusion methods as they are difficult to reach otherwise.

A recent trend in the image registration field is the development of AI methodologies based on deep neural networks[39, 17, 38]. One crucial issue of these methodologies is the definition of robust strategies for generating the samples that are used in the network training step [17]. It is quite common to build these samples by taking image pairs that were registered manually by medical experts with the consequent important investment of time and effort that this requires. We think that our methodology might also be used to generate pairs of registered images that in combination with available and valuable images registered by experts would constitute robust training samples.

The results presented here for our new methodology are, of course, at a preliminary level. Future work should be devised to integrate our methodology into the clinical practice in order to test its real usefulness.

5. Conclusions

In this paper we propose an alternative approach to accurately predict the position of potentially cancerous lesions in the prostate when a TRUS guided biopsy is performed. The proposed methodology

is based on finite element simulations with an accurate and realistic accurate 3-D geometry configuration of the pelvis region. Moreover, our methodology is completely developed on open source software, which means that its implementation would be affordable even for healthcare providers with small budgets.

Abbreviations

3-D: Three-dimensional

AI: Artificial intelligence

CGAL: The Computational Geometry Algorithms Library

CT: computerized tomography

DRE: digital rectal examination

FE: finite element

MRI: magnetic resonance imaging

PCa: prostate cancer

PSA: prostate-specific antigen

PZ: prostate peripheral zone

SMM: statistical motion models

TRUS: transrectal ultrasound

TZ: prostate transitional zone;

Declarations

Ethics approval and consent to participate:

This article does not contain any studies with human participants or animals performed by any of the authors. We used images from the BodyParts 3D database (BodyParts3D, ©The Database Center for Life Science), licensed under Creative Commons Attribution-Share Alike 2.1 Japan. No approval from Ethical Commission was required.

Consent for publication:

No specific informed consent needed.

Availability of data and materials:

Not Applicable.

Competing interests:

The authors declare that they have no competing interests.

Funding:

This project has received funding from the European Union's Horizon 2020 research and innovation programme under the Marie Skłodowska-Curie grant agreement 713679.

Authors' contributions:

Conception and design: C.O., D.P., J.H., J.M.L., G.F., J.R.G.-B.; Development of methodology: M.Q., D.P., J.H., J.M.L., G.F., J.R.G.-B.; Data acquisition (computer simulations): M.Q.; Analysis and interpretation of data: M.Q., D.P., J.H., J.M.L., G.F.; Study supervision: C.O., G.F.; Writing Original Draft: M.Q., D.P., G.F.; Writing-Review and Editing: M.Q., D.P., J.H., J.M.L., G.F., J.R.G.-B.; All authors have read and approved the final manuscript.

Acknowledgements:

The present study has been supported by the Universitat Rovira i Virgili (URV) under Grant 2018PFR-URV-B2-29.

References

1. European Commission. ECIS - European Cancer Information System; 2021. Accessed 25-Jun-2021. <https://ecis.jrc.ec.europa.eu/>.
2. Torre LA, Bray F, Siegel RL, Ferlay J, Lortet-Tieulent J, Jemal A. Global cancer statistics, 2012. *CA: a cancer journal for clinicians*. 2015;65(2):87–108.
3. Rawla P. Epidemiology of prostate cancer. *World journal of oncology*. 2019;10(2):63.
4. Bray F, Ferlay J, Soerjomataram I, Siegel RL, Torre LA, Jemal A. Global cancer statistics 2018: GLOBOCAN estimates of incidence and mortality worldwide for 36 cancers in 185 countries. *CA: a cancer journal for clinicians*. 2018;68(6):394–424.
5. Campbell SC, Lane BR, et al. Malignant renal tumors. *Campbell-Walsh Urology*. 2012;10:1413–74.

6. Palacio-Torralba J, Jimenez Aguilar E, Good DW, Hammer S, McNeill SA, Stewart GD, et al. Patient specific modeling of palpation-based prostate cancer diagnosis: effects of pelvic cavity anatomy and intrabladder pressure. *International journal for numerical methods in biomedical engineering*. 2016;32(1):e02734.
7. Fridhammar A, Axelsson U, Persson U, Bjartell A, Borrebaeck CAK. The Value of a New Diagnostic Test for Prostate Cancer: A Cost-Utility Analysis in Early Stage of Development. *PharmacoEconomics-Open*. 2021;5(1):77–88.
8. Labrie F, Candas B, Dupont A, Cusan L, Gomez JL, Suburu RE, et al. Screening decreases prostate cancer death: first analysis of the 1988 Quebec prospective randomized controlled trial. *Prostate*. 1999;38(2):83–91.
9. Song JM, Kim CB, Chung HC, Kane RL. Prostate-specific antigen, digital rectal examination and transrectal ultrasonography: a meta-analysis for this diagnostic triad of prostate cancer in symptomatic Korean men. *Yonsei medical journal*. 2005;46(3):414.
10. Krouskop TA, Wheeler TM, Kallel F, Garra BS, Hall T. Elastic moduli of breast and prostate tissues under compression. *Ultrasonic Imaging*. 1998;20(4):260–274.
11. Phipps S, Yang TH, Habib FK, Reuben RL, McNeill SA. Measurement of tissue mechanical characteristics to distinguish between benign and malignant prostatic disease. *Urology*. 2005;66(2):447–450.
12. Hoyt K, Castaneda B, Zhang M, Nigwekar P, di Sant’Agnese PA, Joseph JV, et al. Tissue elasticity properties as biomarkers for prostate cancer. *Cancer Biomarkers*. 2008;4(4–5):213–225.
13. Cao R, Huang Z, Varghese T, Nabi G. Tissue mimicking materials for the detection of prostate cancer using shear wave elastography: A validation study. *Medical physics*. 2013;40(2):Article number 022903.
14. Moe A, Hayne D. Transrectal ultrasound biopsy of the prostate: does it still have a role in prostate cancer diagnosis? *Translational Andrology and Urology*. 2020;9(6):3018–3024.
15. Shen F, Shinohara K, Kumar D, Khemka A, Simoneau AR, Werahera PN, et al. Three-dimensional sonography with needle tracking: Role in diagnosis and treatment of prostate cancer. *Journal of Ultrasound in Medicine*. 2008;27(6):895–905.
16. Abdelkhalek M, Abdelshafy M, Elhelaly H, Kamal M. Hemosepermia after transrectal ultrasound-guided prostatic biopsy: A prospective study. *Urology Annals*. 2013;5(1):30–33.
17. Haskins G, Kruecker J, Kruger U, Xu S, Pinto PA, Wood BJ, et al. Learning deep similarity metric for 3D MR-TRUS image registration. *International Journal of Computer Assisted Radiology and Surgery*. 2019;14(3):417–425.
18. Warlick C, Futterer J, Maruf M, George AK, Rastinehad AR, Pinto PA, et al. Beyond transrectal ultrasound-guided prostate biopsies: available techniques and approaches. *World Journal of Urology*. 2019;37:419–427.
19. Wang Y, Ni D, Qin J, Xu M, Xie X, Heng PA. Patient-specific deformation modelling via elastography: application to image-guided prostate interventions. *Scientific Reports*. 2016;6:Article number 27386.

20. Mohamed A, Davatzikos C, Taylor R. A combined statistical and biomechanical model for estimation of intra-operative prostate deformation. *Lecture Notes in Computer Science*. 2002;2489:452–460.
21. Hu Y, van den Boom R, Carter T, Taylor Z, Hawkes D, Ahmed HU, et al. A comparison of the accuracy of statistical models of prostate motion trained using data from biomechanical simulations. *Progress in Biophysics and Molecular Biology*. 2010;103:262–272.
22. Bharatha A, Hirose M, Hata N, Warfield SK, Ferrant M, Zou KH, et al. Evaluation of three-dimensional finite element-based deformable registration of pre- and intraoperative prostate imaging. *Medical Physics*. 2001;28(12):2551–2560.
23. Marchal M, Promayon E, Troccaz J. Simulating prostate surgical procedures with a discrete soft tissue model. In: Mendoza C, Navazo I, editors. 3rd Workshop in Virtual Reality Interactions and Physical Simulations, VRIPHYS 2006. The Eurographics Association; 2006. p. 109–118.
24. Yan D, Jaffray DA, Wong JW. A model to accumulate fractionated dose in a deforming organ. *International Journal of Radiation Oncology Biology Physics*. 1999;44(3):665–675.
25. Keros L, Bernier V, Aletti P, Marchesi V, Wolf D, Noel A. Qualitative estimation of pelvic organ interactions and their consequences on prostate motion: Study on a deceased person. *Medical Physics*. 2006;33(6):1902–1910.
26. Boubaker MB, Haboussi M, Ganghoffer JF, Aletti P. Predictive model of the prostate motion in the context of radiotherapy: A biomechanical approach relying on urodynamic data and mechanical testing. *Journal of the Mechanical Behavior of Biomedical Materials*. 2015;49:30–42.
27. Mitsuhashi N, Fujieda K, Tamura T, Kawamoto S, Takagi T, Okubo K. BodyParts3D: 3D structure database for anatomical concepts. *Nucleic Acids Research*. 2009;37(SUPPL. 1):D782-D785.
28. CGAL. The Computational Geometry Algorithms Library; 2017. Accessed 07-May-2021. <http://www.cgal.org>.
29. Geuzaine C, Remacle JF. Gmsh: A 3-D finite element mesh generator with built-in pre- and post-processing facilities. *International journal for numerical methods in engineering*. 2009;79(11):1309–1331.
30. Electricité de France. Finite element code_aster, Analysis of Structures and Thermomechanics for Studies and Research; 1989–2017. Open source on www.code-aster.org.
31. Li C, Guan G, Zhang F, Song S, Wang RK, Huang Z, et al. Quantitative elasticity measurement of urinary bladder wall using laser-induced surface acoustic waves. *Biomedical Optics Express*. 2014;5(12):4313–4328.
32. Christensen MB, Oberg K, Wolchok JC. Tensile properties of the rectal and sigmoid colon: a comparative analysis of human and porcine tissue. *SpringerPlus*. 2015;4(1):Article number 142.
33. Hensel JM, Ménard C, Chung PW, Milosevic MF, Kirilova A, Moseley JL, et al. Development of multiorgan finite element-based prostate deformation model enabling registration of endorectal coil magnetic resonance imaging for radiotherapy planning. *International Journal of Radiation Oncology Biology Physics*. 2007;68(5):1522–1528.

34. Chai X, van Herk M, van de Kamer JB, Hulshof MCCM, Remeijer P, Lotz HT, et al. Finite element based bladder modeling for image-guided radiotherapy of bladder cancer. *Medical Physics*. 2011;38(1):142–150.
35. Brock KK, Ménard C, Hensel J, Jaffray DA. A multi-organ biomechanical model to analyze prostate deformation due to large deformation of the rectum. In: *Medical Imaging 2006: Physiology, Function, and Structure from Medical Images*. Proceedings of the SPIE. vol. 6143. International Society for Optics and Photonics; 2006. p. 360–369.
36. Ramezani M, Klima S, Le Clerc de la Herverie P, Campo J, Le Joncour JB, Rouquette C, et al. In silico pelvis and sacroiliac joint motion: refining a model of the human osteoligamentous pelvis for assessing physiological load deformation using an inverted validation approach. *BioMed Research International*. 2019;2019:Article number 3973170.
37. Islam T, Tang S, Liverani C, Saha S, Tasciotti E, Righetti R. Non-invasive imaging of Young's modulus and Poisson's ratio in cancers in vivo. *Scientific Reports*. 2020;10(1):Article number 7266.
38. Igarashi R, Koizumi N, Nishiyama Y, Tomita K, Shigenari Y, Shoji S. Sagittal alignment in an MR-TRUS fusion biopsy using only the prostate contour in the axial image. *ROBOMECH Journal*. 2020;7:Article number 4.
39. Wu G, Kim M, Wang Q, Munsell BC, Shen D. Scalable High-Performance Image Registration Framework by Unsupervised Deep Feature Representations Learning. *IEEE Transactions on Biomedical Engineering*. 2016;63(7):1505–1516.

Tables

Table 1

Material properties of the elements in our model for the pelvic region: Elastic modulus (E), Poisson's ratio (η) and density (ρ).

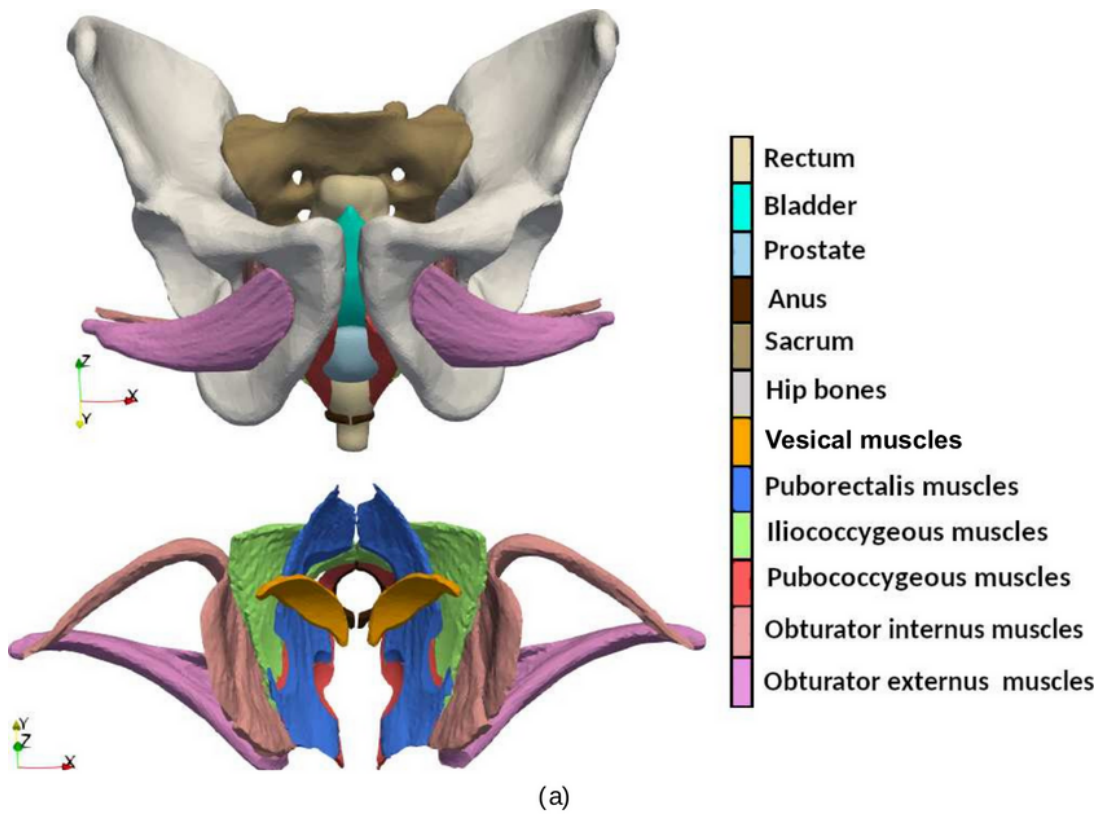
Organ	E (kPa)	η	ρ (kg/m ³)	Source
Prostate transitional zone	43	0.495	1500	[19]
Prostate peripheral zone	18	0.495	1500	[19]
Bladder	10	0.499	1500	[31]
Rectum	5180	0.499	1500	[32]
Anus	10	0.499	1500	[33, 34]
Obturator internus muscles	15	0.4	1500	[33, 34]
Obturator externus muscles	15	0.4	1500	[33, 34]
Iliococcygeous muscles	15	0.4	1500	[33, 34]
Pubococcygeous muscles	15	0.4	1500	[33, 34]
Puborectalis muscles	15	0.4	1500	[33, 34]
Vesical muscles	150	0.4	1000	[35]
Sacrum bones	11×10^6	0.26	1640	[36]
Hip bones	11×10^6	0.26	1640	[36]

Table 2

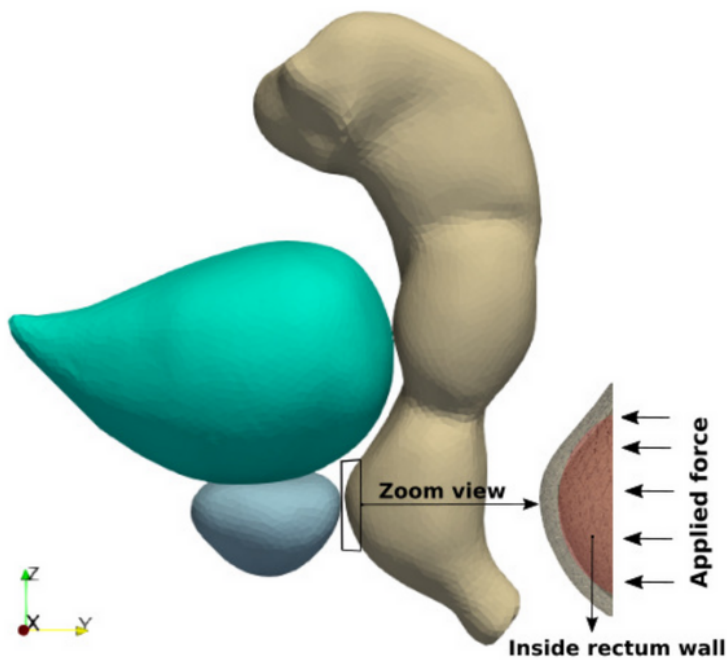
Coordinate displacements and their magnitudes of prostate lesions w.r.t. nodes after applying TRUS pressure at rectum wall.

Node	Location in prostate	Displacements (mm)			
		DX	DY	DZ	Magnitude
N1	PZ midsagittal, intermediate level	0.94	-12.91	5.16	13.93
N2	TZ midsagittal, intermediate level	-0.66	-7.84	2.52	8.26
N3	PZ lateral, intermediate level	3.37	-4.56	1.70	5.20
N4	PZ midsagittal, apex level	0.68	-6.56	1.56	6.78
N5	PZ midsagittal anterior, intermediate level	0.34	-5.53	0.94	5.61

Figures



(a)



(b)

Figure 1

(a) Transverse view of the geometry model for the pelvic region. For the sake of clarity only the involved muscles are included in the bottom plot. Note that in the frontal body view the X-axis points to the right, the Y-axis points toward the dorsal region and the Z-axis points upwards (into the cranial region). (b) Lateral view of the rectum, bladder and prostate organs with a magnification of the interior region of the rectum where the TRUS probe exerts pressure.

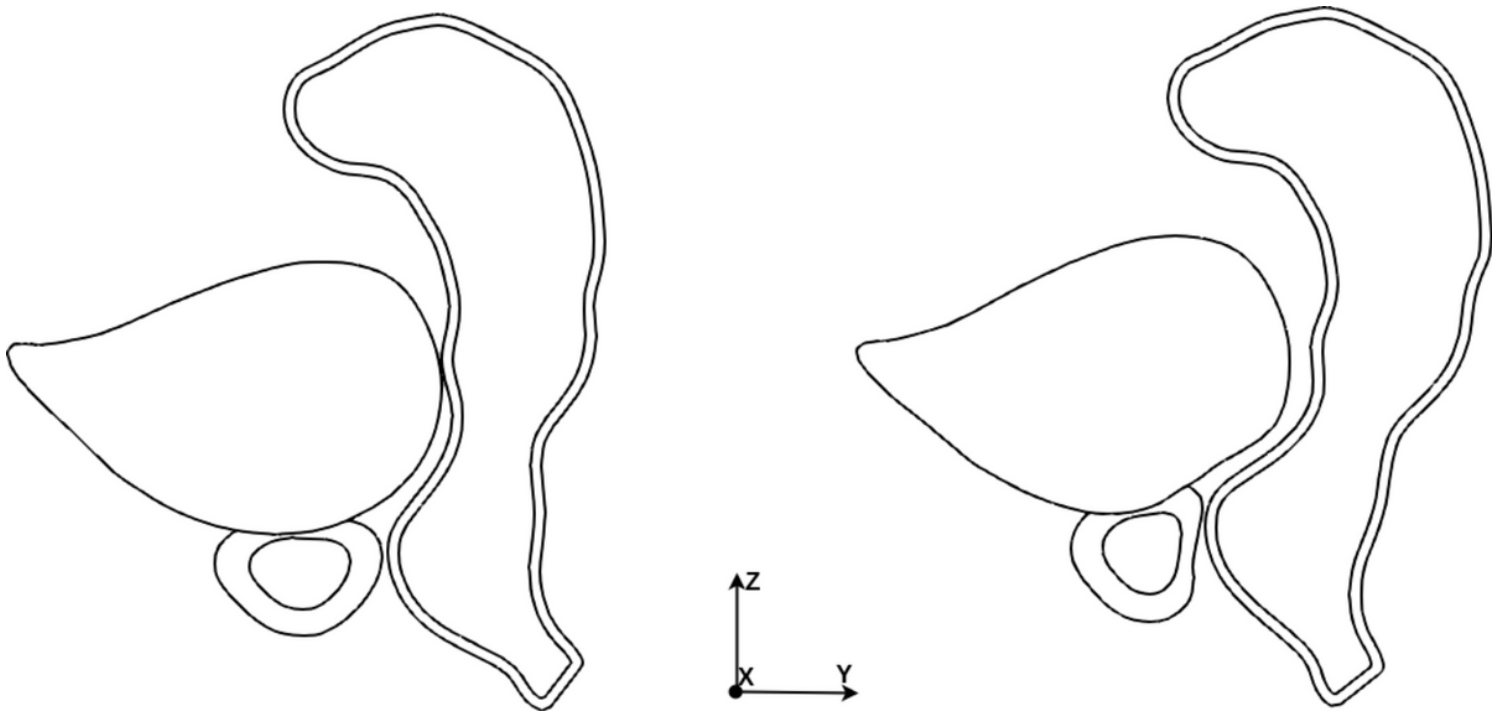


Figure 2

Profiles of the prostate transitional zone (TZ), prostate peripheral zone (PZ), bladder and rectum in the medial ($X = 0$) plane: original (left) and deformed (right) geometries.

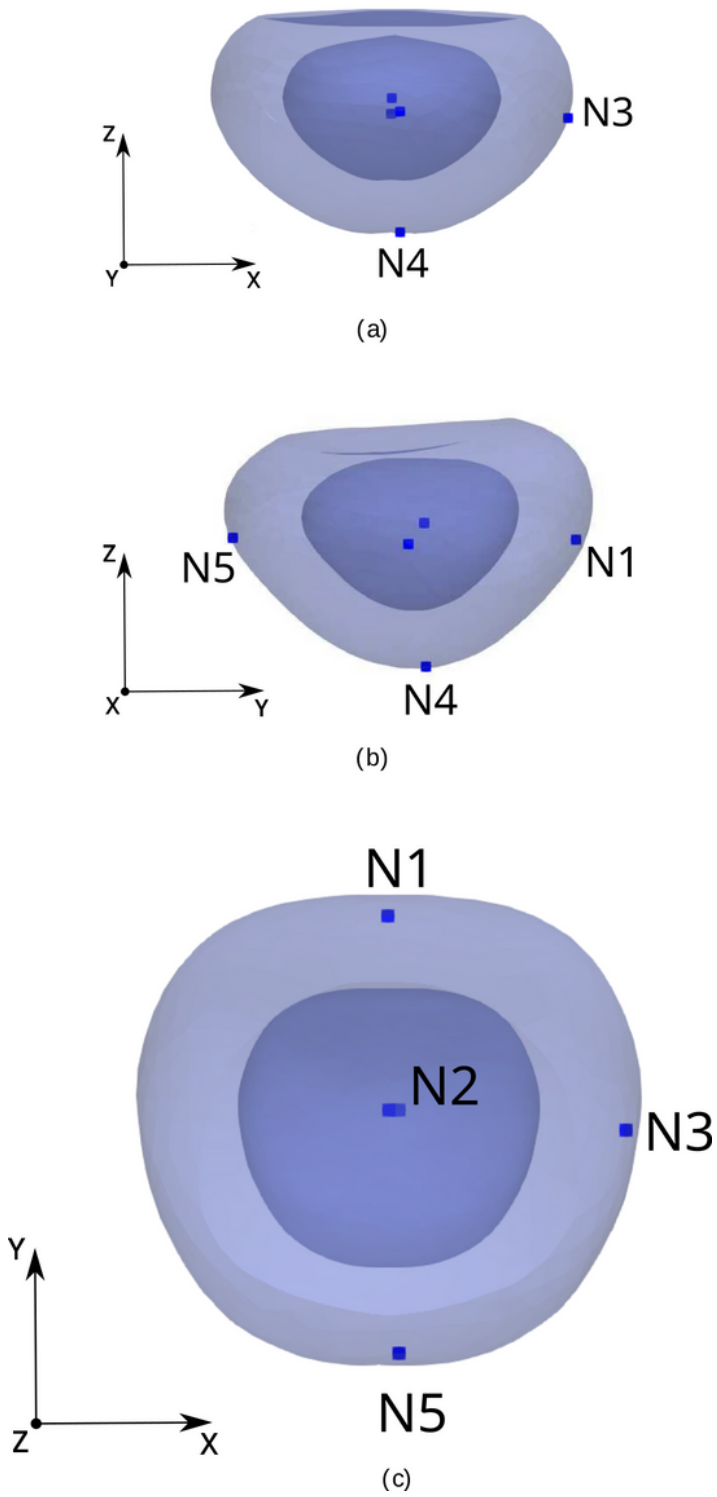


Figure 3

Location of the five selected nodes (potentially cancerous lesions) in the prostate. (a) Coronal (posterior) view. (b) Sagittal view. (c) Axial view.

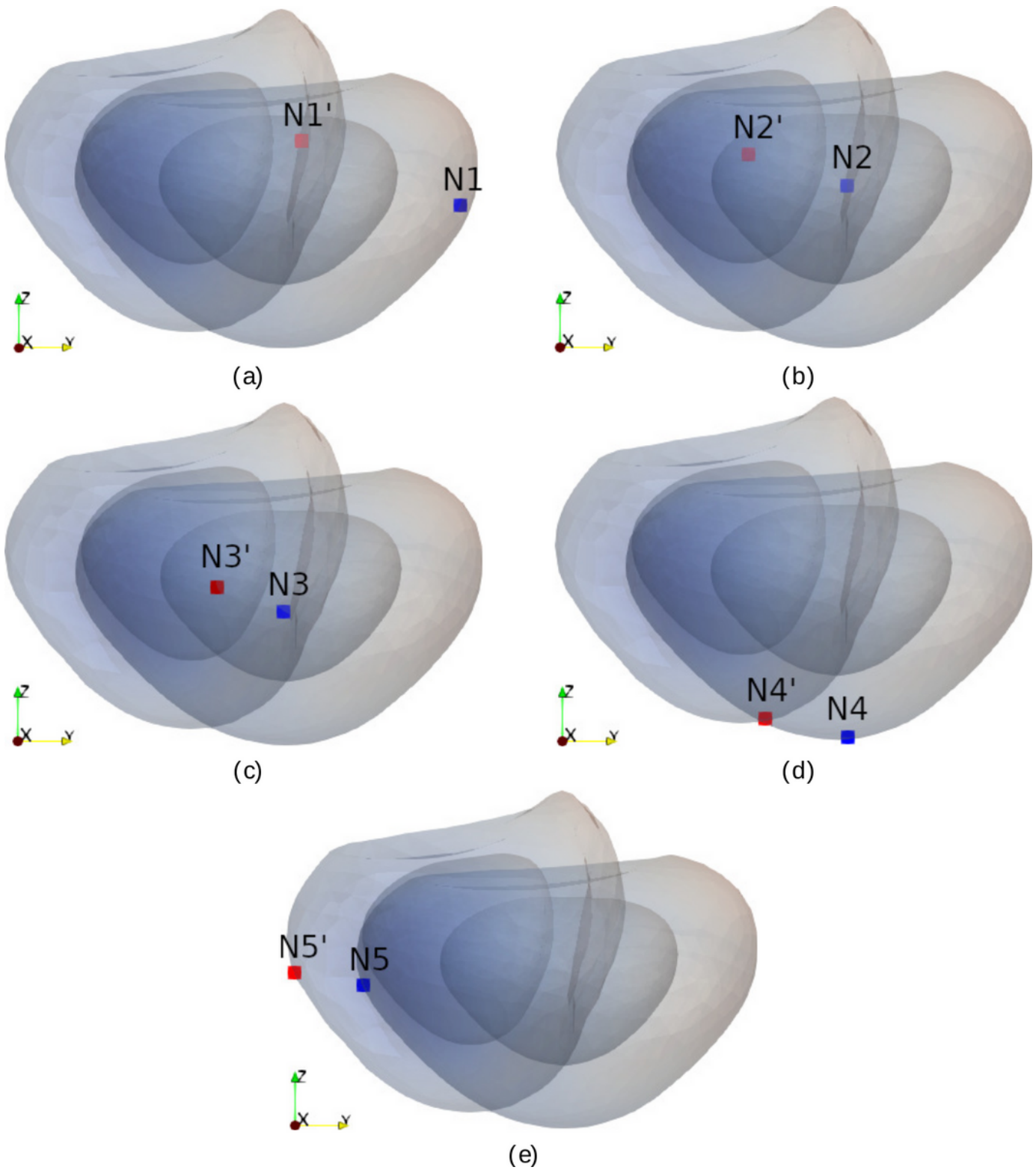


Figure 4

Each plot shows the projection of the 3-D original and deformed prostate surfaces into the sagittal plane. Blue and red squares respectively denote the initial and final locations of each the five selected nodes: (a) N1, (b) N2, (c) N3, (d) N4 and (e) N5. Note that for the sake of clarity final locations are denoted with a prime added to the node label.

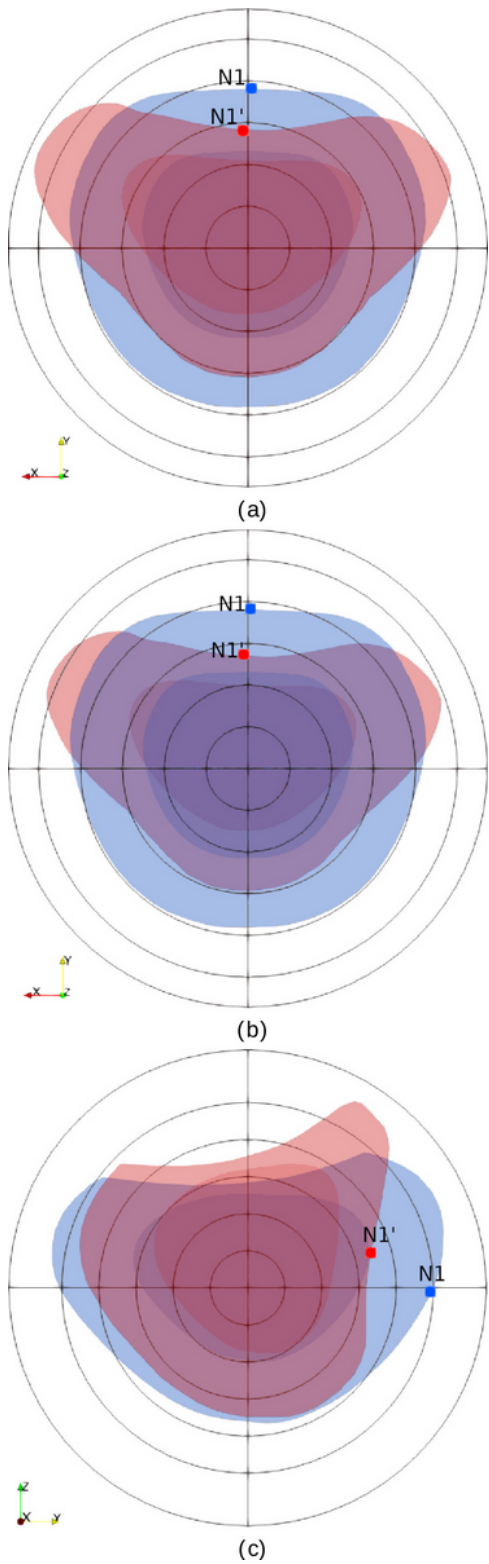


Figure 5

Superposition of Original (blue) and deformed prostate in polar coordinates. (a) Axial views with $Z = 0$ for both original and deformed prostate. (b) Axial views taken at the plane where N1 (N10) is located for the original (deformed) prostate. (c) Sagittal views taken at the plane where N1 (N10) is located for the original (deformed) prostate.